# Optimization of device geometry in single-plate digital microfluidics

Mohamed Abdelgawad,[1] Philip Park,[2,3] and Aaron R. Wheeler[2,a)]
[1]*Department of Mechanical and Industrial Engineering, University of Toronto, 5 King's College Road, Toronto, Ontario M5S 3G8, Canada*
[2]*Department of Chemistry, University of Toronto, 80 St. George Street, Toronto, Ontario M5S 3H6, Canada*
[3]*Department of Physics, University of Toronto, 60 St. George St., Toronto, Ontario M5S 1A7, Canada*

(Received 26 November 2008; accepted 13 March 2009; published online 12 May 2009)

Digital microfluidics is a popular tool for lab-on-a-chip applications and is typically implemented in one of two formats: single-plate ("open") devices or two-plate ("closed") devices. Single-plate devices have some advantages relative to the more common two-plate format such as faster mixing, the capacity to move larger volumes on a given footprint, and easier access to droplets for handling or optical detection. In contrast with the two-plate format, in which ground potential is generally supplied via a top electrode, in the single-plate format, many different geometries of ground wires/electrodes have been used. Until the present study, there has been no metric to determine which of these geometries is best suited for droplet actuation. Here, we present a combination of numerical simulations and experimental tests to compare six different single-plate designs. We applied finite element analysis, using the commercially available COMSOL software package to calculate the electrodynamic actuation forces in each of the different designs and used the results to optimize device design. Forces predicted by the electrodynamic model were in agreement with forces predicted using electromechanical models. More importantly, results were verified experimentally using a unique technique that permits indirect estimation of actuation forces on digital microfluidic devices. This work illustrates the promise of using numerical modeling to enhance the design and performance of digital microfluidic devices. © *2009 American Institute of Physics*.
[DOI: 10.1063/1.3117216]

## I. INTRODUCTION

Digital microfluidics is a fluid-handling technique in which discrete liquid droplets are manipulated on an array of electrodes.[1–3] In this technique, droplets serve as microreactors and can be used to implement low-volume biological applications, such as enzyme assays,[4–6] cell-based assays,[7] polymerase chain reaction (PCR),[8] DNA enrichment[9] and ligation,[10] and proteomics.[11–14] In contrast with the more conventional geometry of enclosed microchannels, digital microfluidics has the capacity to precisely control the position of many different reagents simultaneously, because it does not suffer from unwanted hydrostatic[15] or capillary[16] flows.

There are two digital microfluidic device formats: two-plate (closed) devices and single-plate (open) devices. In two-plate devices,[1,2,8,11–13] which are more common, droplets are sandwiched between two substrates; the bottom one carries the actuation electrode array while the top one comprises the ground electrode. This configuration is capable of performing the four critical fluidic processes of dispensing, splitting, moving, and merging droplets.[17] In single-plate devices,[9,18–21] droplets are actuated on a single substrate that carries both the actuation and grounding electrodes. While, single-plate actuation lacks the capacity to dispense or split droplets (except under very specific conditions[22]), it has advantages such as better mixing of droplet contents upon merging,[18] the ability to move larger droplets per sample footprint, more sensitive optical detection,[20] and faster evaporation, which is useful in applications requiring drying analytes onto the surface.[12]

Since there is no predefined geometry for positioning ground electrodes relative to actuation electrodes in single-plate devices, a wide range of designs employing different strategies have been reported.[18–21,23,24] Changing the position of the grounding electrodes/wires on the device will change the intensity and distribution of the electric field in the vicinity of the droplet, which, in turn, should change the actuation force on the droplet and the maximum droplet speed that can be achieved. However, until now, there have been no studies on the optimum design of such devices. This is likely a result of (a) the time and cost that would be required to experimentally evaluate the different geometries and (b) a lack of accessible and verifiable numerical modeling tools that can compare the different designs. Although some work on modeling digital microfluidics have been reported, most of these studies used in-house written codes[25,26] or available source codes that require the writing of long and complex scripts[27,28] to model each problem. Both these approaches are beyond the reach of researchers in the biochemical and biomedical fields where this technology is most used.

Here we report, for the first time, the use of a commercial modeling package to evaluate single-plate digital microfluidic device designs. In this work, we used electrodynamic[25,29–31] rather than electrowetting[26,27] or electromechanical[32,33] models to calculate actuation forces on droplets approximated as spherical caps with unchanging

a)Author to whom correspondence should be addressed. Electronic mail: awheeler@chem.utoronto.ca. Tel.: (416) 946-3864. FAX: (416) 946-3865.

 

TABLE I. Geometrical configuration of the six designs tested in this study. Energized electrodes are colored red, ground electrodes/wires are colored blue, and floating electrodes are colored gray.

| Design | Description | 3D view | Side view |
|---|---|---|---|
| Fouillet and Achard | Ground potential connected to a wire passing through droplet. | 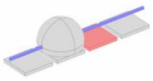 | 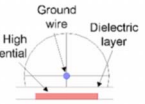  |
| Fair et al. | Ground potential connected to a mesh of wires surrounding the actuation electrodes on top of the dielectric coating | 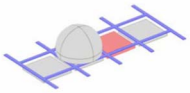 | 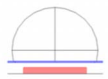 |
| Cooney et al. | Ground potential connected to a wire positioned on top of the dielectric coating in the middle of actuation electrodes. | 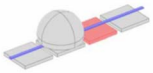 | 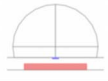 |
| Abdelgawad et al. | Ground potential connected to a line of electrodes parallel to actuation electrodes. |  |  |
| Paik et al. | Ground potential connected to two wires on both sides of actuation electrodes underneath the dielectric coating. | 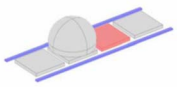 |  |
| Yi and Kim | Ground potential connected to a line of electrodes parallel to the actuation ones underneath the dielectric coating | 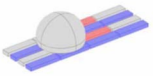 |  |

geometry (i.e., no wetting or contact angle change). We note that electrodynamic and electrowetting/mechanical models are not mutually exclusive, as contact angle change in electrowetting can be interpreted as an equilibrium between electrodynamic forces and surface tension.[25,30,34–36] In this work, we solved for the electric field around the droplet and calculated the charge density accumulated on droplet surfaces for six single-plate designs reported in the literature[9,18–21,24] and then we used the Maxwell-stress tensor formulation to calculate the droplet actuation forces in each design. We validated the modeling results experimentally by estimating the forces acting on droplets in devices corresponding to three of the modeled designs using a unique measurement technique. Finally, the modeling results were used to generate a list of design tips for production of devices with maximum actuation forces. We posit that tools such as these can help researchers (even those without extensive modeling experience) rapidly design devices with higher actuation forces and, consequently, faster droplet motion.

## II. PROBLEM DESCRIPTION

### A. Geometrical parameters

Table I shows the six different designs evaluated in the present work. In each case, we modeled the electric field distribution and calculated the actuation forces on the droplet. To ensure fair comparison between all designs, all relevant parameters—droplet volume, electrode dimensions, dielectric coating thickness, electrode spacing, static contact angle, droplet base radius, physical properties, and applied voltage—were held constant. Figure 1 and Table II show electrode dimensions and droplet properties used in this study.

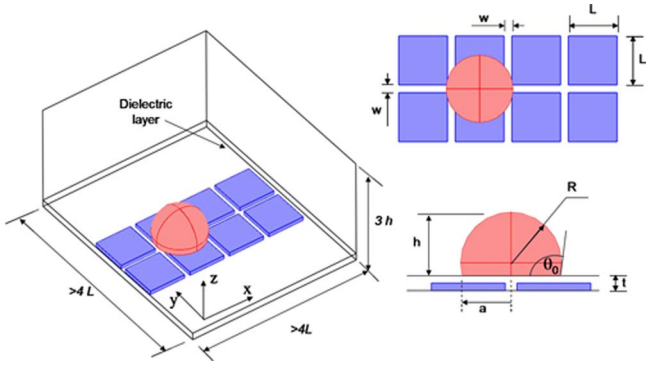


FIG. 1. (Color online) Schematic of one of the modeled devices (Ref. 9); electrodes and droplet dimensions were fixed in all cases to ensure accurate comparison between different designs. All dimensions are listed in Table II.

### B. Governing equations

To calculate the electric field and charge distribution on droplets in digital microfluidic devices, we solved the conservation of charge Eq. (1) and the Laplace Eq. (2) in the droplet and its surrounding media,

$$\nabla(\sigma \nabla V) = 0, \tag{1}$$

$$\nabla(\varepsilon \nabla V) = 0, \tag{2}$$

where $\varepsilon = \varepsilon_r \varepsilon_0$ ($\varepsilon_r$ is the relative permittivity of the medium and $\varepsilon_0$ is permittivity of vacuum), $\sigma$ is the electrical conductivity of the droplet, and $V$ is the electric potential. Droplets were approximated as nondeformable spherical caps, so there was no need to solve the Navier–Stokes equation. Actuation forces were calculated by integrating the electrodynamic forces per unit volume over the whole droplet according to Eq. (3), assuming negligible magnetic fields,[29]

$$\mathbf{F} = \int_V \varepsilon(\nabla \cdot \mathbf{E})\mathbf{E} + \varepsilon(\mathbf{E} \cdot \nabla)\mathbf{E} - 0.5\nabla(\varepsilon \mathbf{E}^2) dv, \tag{3}$$

where $\mathbf{F}$ is the actuation force vector and $\mathbf{E}$ is the electric field.

TABLE II. Electrode dimensions and physical properties used in all designs.

| Parameter | Value |
|---|---|
| Electrode dimensions ($L \times L$) | $1 \times 1$ mm$^2$ |
| Electrode spacing ($w$) | 40 $\mu$m |
| Dielectric thickness ($t$) | 10 $\mu$m |
| Ground line width/diameter (not shown in Fig. 1) | 100 $\mu$m |
| Ground wire radius ($r$) | 50 $\mu$m |
| Droplet volume | 1 $\mu$l |
| Droplet radius ($R$) | 702 $\mu$m |
| Droplet base radius ($a$) | 678 $\mu$m |
| Droplet height ($h$) | 880 $\mu$m |
| Static contact angle ($\theta_0$) | 105° |
| Droplet conductivity ($\sigma$) | $5.5 \times 10^{-6}$ S/m |
| Relative permittivity of droplet | 80 |
| Relative permittivity of air | 1 |
| Relative permittivity of dielectric coating (parylene-C) | 2.65 |
| Permittivity of vacuum | $8.54 \times 10^{-12}$ F/m |
| Contact angle hysteresis | 23° |

Equation (3) can be simplified if tensor notation is used and the volume integral is transformed to a surface integral using the Gauss theorem.[29] The resulting equation becomes

$$\mathbf{F} = \int_S \mathbf{T} \cdot \mathbf{n} ds, \tag{4}$$

$$\mathbf{T}_{ij} = \varepsilon(E_i E_j - 0.5\delta_{ij} E^2), \tag{5}$$

which is the well-known Maxwell-stress tensor that has been used in some previous modeling of digital microfluidics.[34,35] In Eqs. (4) and (5), $\mathbf{T}_{i,j}$ is the Maxwell stress tensor, where $i$ and $j$ refer to pairs of $x$, $y$, and $z$ axes, $\delta_{ij}$ is the Kronecker delta, and $E$ is the electric field surrounding the droplet.

### C. Boundary conditions

A driving potential ($V$=700 V dc) was applied to the actuation electrode in front of the droplet. Ground potential ($V$=0 V) was applied to ground electrodes/wires. All other external boundaries were set to have electrical insulation ($\mathbf{n}\cdot\mathbf{J}=0$) for the charge conservation Eq. (1) and zero-charge/symmetry ($\mathbf{n}\cdot\mathbf{D}=0$) for the Laplace Eq. (2), where $\mathbf{J}$ is the current density, $\mathbf{D}$ is the electric displacement, and $\mathbf{n}$ is the unit vector normal to the surface. In symmetrical designs (i.e., all designs except that of Abdelgawad *et al.*[9] and Yi and Kim[20]), only half the geometry was modeled to reduce computational time. In these cases, boundary conditions on the symmetry plane were set to zero-charge/symmetry and electrical insulation for the Laplace equation and conservation of charge equation, respectively. In the Fouillet and Achard case, capillary forces between the droplet and the ground wire passing through it were ignored. On interfaces between the different media in the model (i.e., dielectric-air, droplet-air, and dielectric-droplet), the electric displacement $\mathbf{D}$ and the electric field $\mathbf{E}$ were set to follow boundary conditions (6) for the Laplace equation, while the current density vector $\mathbf{J}$ was set to fulfill the continuity boundary conditions (7),

$$\mathbf{n}\cdot(\mathbf{D}_1 - \mathbf{D}_2) = \rho_s \quad \text{and} \quad \mathbf{n}\times(\mathbf{E}_1 - \mathbf{E}_2) = 0, \tag{6}$$

$$\mathbf{n}\cdot[(\sigma\nabla V)_1 - (\sigma\nabla V)_2] = -\mathbf{n}\cdot(\mathbf{J}_1 - \mathbf{J}_2) = 0, \tag{7}$$

where $\rho_s$ is the surface charge density. Electrode thickness was not modeled (to reduce mesh size and computation time), which is reasonable because electrodes in actual devices are typically much thinner (~100 nm) than dielectric layer thicknesses (~1–10 $\mu$m). Not simulating the electrode thickness accounted for an error of less than 5% in the total actuation force based on one case in which electrode thickness was simulated.

The final overall dimensions of the modeled designs were determined by evaluating a series of cases with different lengths, widths, and heights starting with largest geometry and reducing the model size gradually until the results converged on a model large enough to simulate infinite space with reasonable accuracy without unnecessary waste of computational time.

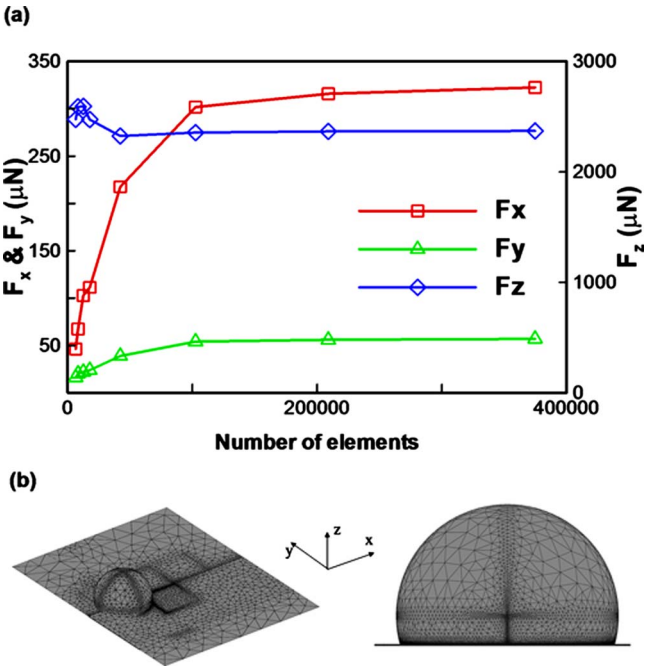


FIG. 2. (Color online) (a) Electrodynamic forces ($F_x$, $F_y$, and $F_z$) as a function of the number of elements. (b) Pictures of the mesh used in the Abdelgawad *et al.* case.

### D. Numerical methods

The conservation of charge and Laplace equations were solved on modeled geometries using the COMSOL 3.4 (Burlington, MA) finite element package. We used a Lagrange-quadratic element type and the conjugate gradients[37] iterative stationary solver. The relative tolerance used as a convergence criterion was tol.$=10^{-6}$ in Eq. (8),

$$\rho|M^{-1}(b - Ax)| < \text{tol.}|M^{-1}b|, \tag{8}$$

where $\rho$ is the factor in error estimate ($\rho$=400 in the current study), $M$ is the preconditioner matrix, $Ax=b$ is the system of equations to be solved, and tol. is the relative tolerance. To speed up convergence, we used a $V$-cycle multigrid[38] with six levels. The UMFPACK direct solver[39] was used on the coarsest mesh to get a more accurate correction for finer mesh levels.

### E. Mesh independence

In initial tests, different meshes were used to determine the optimum mesh size and to ensure a mesh-independent solution. Figure 2(a) shows the effect of number of elements on the electrodynamic forces acting in the $x$, $y$, and $z$ directions ($F_x$, $F_y$, and $F_z$), on the droplet in the first case in Table I (Fouillet and Achard[21]); as shown, convergence was reached at about 200 000 elements. This mesh corresponds to an element size of about 2 $\mu$m near the three-phase line and increases gradually away from that region, and is shown in Figure 2(b).

## III. EXPERIMENTAL

### A. Materials

Chemicals used for photolithography included Shipley-S1811 photoresist and MF-321 developer (Rohm and Hass, Marlborough, MA), hexamethyldisilazane (HMDS) primer (Shin-Etsu MicroSi, Phoenix, AZ), and photoresist stripper AZ300T (AZ Electronic Materials, Somerville, NJ). Chromium pellets for e-beam coating were obtained from Kurt J. Lesker Canada (Toronto, ON) and CR-4 Chromium etchant from Cyantek (Fermont, CA). Parylene-C dimer was obtained from Specialty Coating Systems (Indianapolis, IN) and Teflon-AF from DuPont (Wilmington, DE).

### B. Device fabrication

Digital microfluidic devices were formed by photolithography and etching as described previously.[7] Briefly, glass slides were cleaned in piranha solution (3:1 sulfuric acid:hydrogen peroxide by volume) for 10 min and coated with 150 nm thick layer of chromium by electron beam deposition (BOC Edwards, Wilmington, MA). After rinsing [acetone, methanol, de-ionized (DI) water] and baking on a hot plate (115 °C, 5 min), substrates were primed by spin coating with HMDS (3000 rpm, 30 s) and then spin coated with Shipley S1811 photoresist (3000 rpm, 30 s). Substrates were baked on a hot plate (100 °C, 2 min) and exposed (35.5 $mW/cm^2$, 4 s) through a transparency photomask (City Graphics, Toronto, ON) using a Karl Suss MA6 mask aligner (Garching, Germany). Then substrates were developed (MF321, 3 min) and postbaked on a hot plate (100 °C, 1 min). After photolithography, exposed chromium was etched (CR-4, 2 min) and the remaining photoresist was stripped by sonicating the substrates in AZ300T (5 min). A 10 $\mu$m thick layer of parylene-C was then applied by vapor deposition (Specialty Coating Systems, Indianapolis, IN). A final hydrophobic coating (~750 nm thick) was applied by spin coating Teflon-AF (1% by weight in Fluorinert FC-40, 1000 rpm, 1 min) and baking on a hot plate (160 °C, 10 min). For the Fouillet and Achard design and the design suggested by the simulation results, a ground wire was formed from a 200 $\mu$m diameter aluminum wire suspended a few hundred microns above the surface, mounted on wedges on both sides of the device.

### C. Device operation

DI water droplets were actuated in air on single-plate devices by applying electric potentials (18 kHz, $700V_{rms}$) between actuation electrodes and grounding electrodes/wires. Droplet motion was monitored by a charge coupled device camera (KP-D20BU, Hitachi Canada, Mississauga, ON) mated to an imaging lens (Edmund Industrial Optics, Barrington, NJ) positioned over the top of the device.

### D. Measurement of contact angle hysteresis

Contact angle hysteresis was measured by dispensing a 15 $\mu$l droplet on a Teflon coated glass substrate, which was mounted on a variable inclination stage. The substrate was inclined gradually until the droplet started sliding down the substrate, at which point a picture was taken and the advancing and receding contact angles of the droplet were measured. The contact angle hysteresis reported in Table II is the difference between these two angles.

TABLE III. Results of the numerical modeling of the six tested designs; colors represent electric potential. Actuation forces are shown on the third column as short black arrows.

| Design | Potential distribution | Actuation forces on contact line | $F_x$ (μN) |
|---|---|---|---|
| Fouillet and Achard | 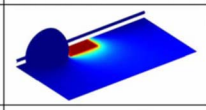 | 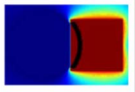 | 316 |
| Fair et al. | 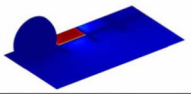 | 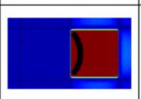 | 309 |
| Cooney et al. | 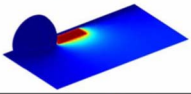 | 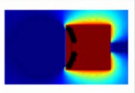 | 237 |
| Abdelgawad et al. | 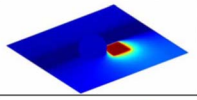 | 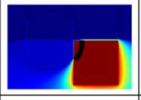 | 134 |
| Paik et al. | 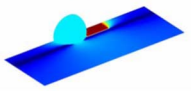 | 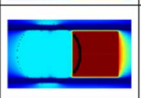 | 132 |
| Yi and Kim | 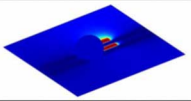 | 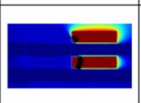 | 80 |
| | 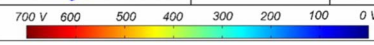  | | |

### E. Experimental comparison of actuation forces on different designs

The maximum droplet volume that can be actuated vertically upward on each device was used as a measure of the electrodynamic forces generated $F_e$ (see detailed explanation in the results). To measure these volumes, a droplet of DI water was pipetted onto the surface of a device oriented vertically with respect to the ground and driven upward at an applied voltage of $700V_{rms}$, over at least four electrodes. After each successful movement, another droplet, 0.5 $\mu$l bigger than the previous one, was tested for actuation feasibility. This was repeated until the driving force was no longer sufficient for the droplet to move. This final droplet volume less 0.5 $\mu$l was deemed the maximum volume that could be actuated. After each initial maximum volume was recorded, at least two additional trials were carried out to confirm the initial results.

## IV. RESULTS AND DISCUSSION

### A. Effect of grounding electrode size and position

We calculated the electrodynamic actuation force in the $x$-direction ($F_x$) acting on a droplet on the six different designs shown in Table I. In each case, the droplet front edge was positioned 200 $\mu$m into the energized electrode; results are shown in Table III. Although forces in the $y$ and $z$ directions ($F_y$ and $F_z$) can be calculated, they are not important in this study as they are not responsible for forward droplet

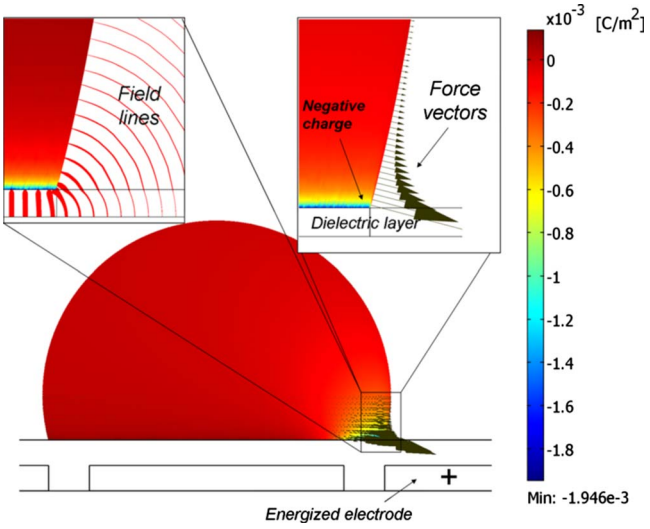


FIG. 3. (Color online) Electrodynamic forces (black arrows) are most dense on the front of the droplet near the three-phase contact line because of negative charge accumulation in this region. The left inset shows electric field lines in the vicinity of the three-phase contact line (line thickness scales with field intensity), whereas the right inset shows the force distribution in the same region (in the vertical plane passing through droplet center).

motion. However, $F_y$ and $F_z$ might be valuable in other contexts for modeling droplet shape changes or for studying internal convection currents.

The different designs generated electrodynamic forces that varied significantly—nearly a factor of 4 between highest and lowest. As shown in Fig. 3, forces were concentrated on the front three-phase contact line (i.e., nearest to the active electrode) because electric field intensity and trapped surface charge density were highest in this region. Forces were highest in designs in which the droplet is grounded (i.e., the droplet is in direct contact with the grounding wire/electrode without a dielectric coating in between) because this increased the intensity of the electric field and charge accumulation at the droplet surface.

The increase in forces for grounded droplets predicted by our electrodynamic model agrees with electromechanical modeling of droplet actuation given by the equation $F_x = 1/2\ cV^2$, where $c$ is the capacitance per unit area and $V$ is the applied voltage.[25] These electromechanical forces are 261, 293, and 703 $\mu$N for the three grounded cases shown in Table III, Fouillet and Achard, Fair *et al.*, and Cooney *et al.*, respectively. As can be seen, these values are close to the electrodynamically calculated forces in Table III, except for that of the third case, Cooney *et al.* In this case, the electromechanical model fails to give an accurate prediction of the actuation forces because the ground wire is positioned between the droplet and the active electrode. This violates one of the fundamental assumptions of the electromechanical model, which implies that the droplet lies in the path of the electric field lines between the active and ground electrodes.[25,31,32,40] The large force indicated by the electromechanical model in this case is spurious, because many of the electrical field lines originate and terminate in the spacing between the active electrode and the ground wire away from the droplet.

A second factor that our electrodynamic model predicts is associated with higher actuation force is the length of the overlapping region of the contact line with the energized electrode. This observation was most apparent in comparing the forces generated in the Cooney *et al.* design relative to the Fouillet and Achard and Fair *et al.* designs (Table III). Although the droplet is grounded in all three designs, the force generated in the Cooney *et al.* device was lower because the ground wire covered the center part of the energized electrode and masked it from the contact line.

For designs in which the droplet is not grounded, i.e., Abdelgawad *et al.*, Paik *et al.*, and Yi and Kim, the droplet potential floated to a value between that of the energized electrode (700 V) and ground and reached values of 46, 205, and 47 V, respectively. In general, droplet potential was dependent on the ground electrode size (the bigger the size, the lower the droplet potential) and on the extent of droplet overlap with the ground electrode(s). In nongrounded droplets, electrodynamic forces were significantly lower (see Table III) and were inversely proportional to the potential the droplet floated to. As was the case for grounded droplets, forces were higher for designs in which a larger fraction of the three-phase contact line overlaps the energized electrode.

We note that Maxwell stress and, consequently, the resulting actuation forces are dependent on the dynamic contact angle of the droplet,[34,36,41] which was not modeled in this study (to avoid the complexity associated with solving the Navier–Stokes equations with a moving mesh). However, since the initial electrodynamic force generated on the static contact angle is responsible for overcoming line pinning on the front contact line, we believe that devices with higher initial forces should provide more efficient actuation even if the force decreases as a consequence of the reduction in the contact angle at the beginning of motion. Thus the actuation force modeled in this study is a reasonable criterion for evaluating device design.

### B. Electrodynamic force dependence on droplet position

Electrodynamic forces were found to change significantly with droplet position relative to the energized electrode. Figure 4(a) shows the electrodynamic force calculated at 14 positions along the droplet path from the original (nonenergized) electrode to the adjacent energized electrode. As the droplet moves, actuation forces start low, increase to a maximum, and then decrease to zero. This trend is correlated with the fraction of the contact line that overlaps the energized electrode. Electrodynamic forces on the contact line are represented as black arrows in Figures 4(b)–4(d). Note that at the final position of the droplet on the center of the energized electrode, reverse forces are generated from the two corners of the electrode behind the droplet. This suggests that it is better to keep electrode length (parallel to droplet motion) shorter than droplet diameter to avoid such reverse forces.

In addition to determining the extent of the energized portion of the contact line, droplet position also has significant effect on droplet potential if the droplet is not grounded.

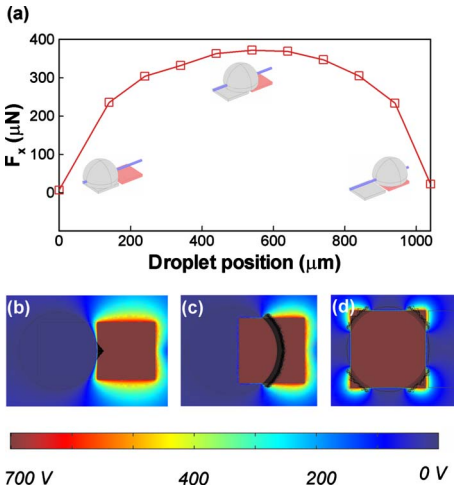


FIG. 4. (Color online) Electrodynamic force dependence on droplet position relative to the energized electrode. (a) Plot of $F_x$ as a function of droplet position for the Fouillet and Achard design. [(b)–(d)] Force distribution (black arrows) on the three-phase contact line at different droplet positions. Note that backward forces are generated by the electrode back corners in (d).

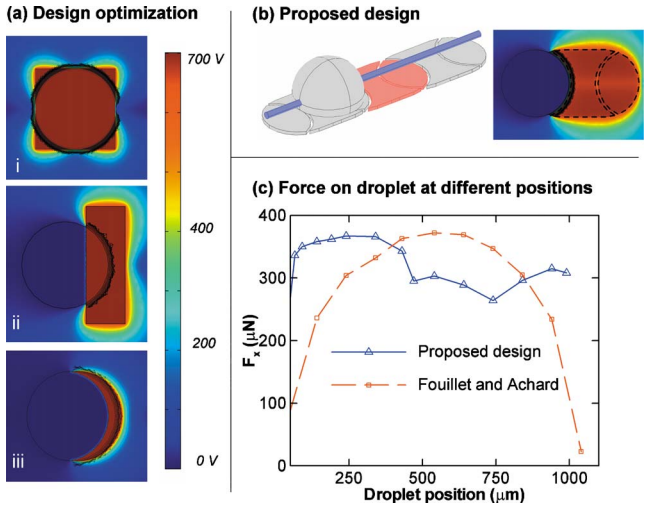


FIG. 5. (Color online) Electrodynamic force dependence on geometry (force distribution represented by black arrows) (a) Design rules to increase actuation forces: the electrode should be short and wide (compare i and ii) to avoid backward forces and to generate forces on a large portion of the front contact line and surround the droplet edge (as in iii) to generate higher forces at the beginning of motion. (b) Proposed optimum electrode design. (c) Plot of $F_x$ as a function of droplet position for the Fouillet and Achard design and the proposed design shown in (b).

In this case, the more the droplet overlaps the electrode, the higher its potential, which reduces the electric field intensity and the electrodynamic forces. This predicted dependence of actuation forces on droplet position agrees with previous studies using energy-based modeling.[42]

### C. Optimization of electrode shape

Careful study of how the electrodynamic force is distributed on the droplet surface and how it changes with droplet position relative to the energized electrode is useful for optimizing device design to achieve high actuation forces. This insight can be summarized in the following four points:

(1) The droplet should be always grounded by direct contact with ground wires/electrodes. This will increase the intensity of the electric field on the front droplet surface and, hence, increase the accumulated charge, generating stronger electrodynamic forces.
(2) The electrode length (parallel to the direction of droplet motion) should be smaller than droplet base diameter, as in Fig. 5(a)(ii), to avoid the generation of forces acting in the reverse direction, as in Fig. 5(a)(i).
(3) The electrode width (normal to the direction of droplet motion) should be larger than the droplet base diameter to generate electrodynamic forces on a large portion of the three-phase contact line, Fig. 5(a)(ii).
(4) The electrode should be shaped to conform with the droplet contact line; this will facilitate larger electrodynamic forces from the beginning of motion, even though it will not increase forces above its maximum, Fig. 5(a)(iii).

We used these four tips to develop an optimum electrode design, shown in Fig. 5(b), which generates higher electrodynamic forces from the beginning of motion and is capable of maintaining these forces during droplet translation. In this design, the electrode is split into two portions; the first is concave on both sides to facilitate application of forces to the entire droplet front, while the second is convex to maintain the highest forces while the droplet moves to the next concave electrode. Figure 5(c) shows that this optimum design can maintain a more uniform force distribution along droplet path compared to the straight-sided electrodes.

### D. Experimental verification

To validate the predicted results, we developed a unique method to compare actuation forces experimentally. Because there is no convenient method to directly measure forces on droplets being actuated, we estimated them indirectly as a function of the resistive forces they overcome. When a droplet is actuated by digital microfluidics on a vertical surface, there are three forces affecting motion: electrodynamic force $F_e$, friction force $F_f$, and droplet weight $W$, Fig. 6(a). As described in the preceding sections, the $F_e$ is determined by the electric field intensity and accumulated surface charge, and to a lesser extent, the droplet volume [droplet volume only affects the length of the contact line overlapping the energized electrode which can be neutralized if electrode width ($w$) is larger than droplet base diameter]. Friction force $F_f$ results mainly from line pinning (i.e., contact angle hysteresis)[26,43] rather than viscous friction[44,45] and increases gradually with droplet volume.[9] Finally, droplet weight increases linearly with droplet volume. This means that the driving force is nearly independent of droplet volume, whereas resistive forces increase significantly with the volume. Thus, for a certain applied voltage and device geometry, there should be a maximum volume that can be actuated vertically upward; the higher the electrodynamic force, the bigger this maximum volume. Based on this analysis, the

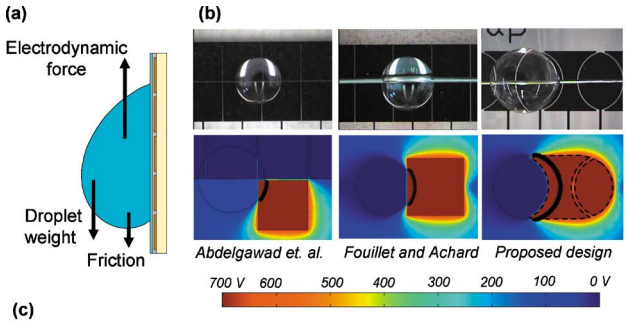


(c)

| Device | Abdelgawad et al. | Fouillet and Achard | Proposed design |
|---|---|---|---|
| Calculated force | 134 μN | 316 μN | 367 μN |
| Theoretical volume to move up with no friction | 13.7 μL | 32.2 μL | 37.4 μN |
| Experimental droplet volume | 8 μL | 14 μL | 17 μL |

FIG. 6. (Color online) Experimental verification of simulation results. (a) Schematic depicting forces affecting vertical motion of a droplet. (b) Pictures (top) and simulation results (bottom, force distribution represented by black arrows) of the devices that were tested. (c) Table of maximum volumes that can be driven upward using each design. The trend in this measurement matches the trend in calculated forces.

maximum actuatable droplet volume up a vertical device surface was the experimental criterion used to compare electrodynamic forces.

For experimental verification we selected three designs that were most easily fabricated, Fig. 6(b): Abdelgawad *et al.*, Fouillet and Achard, and the concave/convex design proposed in the previous section. As listed in Fig. 6(c), the maximum droplet volumes that can be actuated on the different devices are quite different, indicating that electrode design and device geometry have significant effect on the electrodynamic forces. Moreover, the experimental observations match the trend of the predicted device performance, which suggests that electrodynamic modeling can be used to guide device design and fabrication. We speculate that future models can approximate the experimental results more accurately by coupling electrodynamics with mechanical models of friction forces (line pinning) and droplet shape changes.

## V. CONCLUSION

Electrodynamic modeling is a comprehensive tool that can be used to study droplet actuation in digital microfluidics and can be carried out using commercial numerical simulation packages, which do not require extensive programming expertise. Using this tool, we found that there is significant variation in actuation forces among the various designs reported in the literature for single-plate droplet manipulation. Higher actuation forces can be achieved if electrodes are wider, shorter, and possess circular edges, and when the droplet is grounded. Most importantly, experimental results agreed with the modeling results, which suggest utility in device design and fabrication.

[1]J. Lee, H. Moon, J. Fowler, T. Schoellhammer, and C.-J. Kim, Sens. Actuators, A **95**, 259 (2002).
[2]M. G. Pollack, R. B. Fair, and A. D. Shenderov, Appl. Phys. Lett. **77**, 1725 (2000).
[3]M. Washizu, IEEE Trans. Ind. Appl. **34**, 732 (1998).
[4]V. Srinivasan, V. K. Pamula, and R. B. Fair, Lab Chip **4**, 310 (2004).
[5]T. Taniguchi, T. Torii, and T. Higuchi, Lab Chip **2**, 19 (2002).
[6]E. M. Miller and A. R. Wheeler, Anal. Chem. **80**, 1614 (2008).
[7]I. Barbulovic-Nad, H. Yang, P. S. Park, and A. R. Wheeler, Lab Chip **8**, 519 (2008).
[8]Y.-H. Chang, G.-B. Lee, F.-C. Huang, Y.-Y. Chen, and J.-L. Lin, Biomed. Microdevices **8**, 215 (2006).
[9]M. Abdelgawad, S. L. Freire, H. Yang, and A. R. Wheeler, Lab Chip **8**, 672 (2008).
[10]Y.-J. Liu, D.-J. Yao, H.-C. Lin, W.-Y. Chang, and H.-Y. Chang, J. Micromech. Microeng. **18**, 045017 (2008).
[11]H. Moon, A. R. Wheeler, R. L. Garrell, J. A. Loo, and C. J. Kim, Lab Chip **6**, 1213 (2006).
[12]A. R. Wheeler, C. A. Bird, J. A. Loo, R. L. Garrell, R. R. O. Loo, C. J. Kim, and H. Moon, Anal. Chem. **77**, 534 (2005).
[13]A. R. Wheeler, H. Moon, C. J. Kim, J. A. Loo, and R. L. Garrell, Anal. Chem. **76**, 4833 (2004).
[14]V. N. Luk, G. C. Mo, and A. R. Wheeler, Langmuir **24**, 6382 (2008).
[15]H. J. Crabtree, E. C. S. Cheong, D. A. Tilroe, and C. J. Backhouse, Anal. Chem. **73**, 4079 (2001).
[16]G. M. Walker and D. J. Beebe, Lab Chip **2**, 131 (2002).
[17]S. K. Cho, H. Moon, and C. J. Kim, J. Microelectromech. Syst. **12**, 70 (2003).
[18]C. Cooney, C.-Y. Chen, M. Emerling, A. Nadim, and J. Sterling, Microfluid. Nanofluid. **2**, 435 (2006).
[19]P. Y. Paik, V. K. Pamula, and K. Chakrabarty, IEEE Trans. Very Large Scale Integr. (VLSI) Syst. **16**, 432 (2008).
[20]U.-C. Yi and C.-J. Kim, J. Micromech. Microeng. **16**, 2053 (2006).
[21]Y. Fouillet and J. L. Achard, C. R. Phys. **5**, 577 (2004).
[22]J. Berthier, *Microdrops and Digital Microfluidics* (William Andrew, Norwich, NY, 2008).
[23]M. Abdelgawad and A. R. Wheeler, Adv. Mater. (Weinheim, Ger.) **19**, 133 (2007).
[24]R. B. Fair, A. Khlystov, V. Srinivasan, V. K. Pamula, and K. N. Weaver, Proc. SPIE **5591**, 113 (2004).
[25]E. Baird, P. Young, and K. Mohseni, Microfluid. Nanofluid. **3**, 635 (2007).
[26]S. W. Walker and B. Shapiro, J. Microelectromech. Syst. **15**, 986 (2006).
[27]J. Lienemann, A. Greiner, and J. G. Korvink, IEEE Trans. Comput.-Aided Des. **25**, 234 (2006).
[28]J. Berthier, P. Clementz, O. Raccurt, D. Jary, P. Claustre, C. Peponnet, and Y. Fouillet, Sens. Actuators, A **127**, 283 (2006).
[29]D. J. Griffiths, *Introduction to Electrodynamics*, 3rd ed. (Prentice-Hall, Upper Saddle River, NJ, 1999).
[30]J. Zeng and T. Korsmeyer, Lab Chip **4**, 265 (2004).
[31]P. M. Young and K. Mohseni, ASME Trans. J. Fluids Eng. **130**, 081603 (2008).
[32]K. L. Wang, T. B. Jones, and A. Raisanen, J. Micromech. Microeng. **17**, 76 (2007).
[33]T. B. Jones, J. Micromech. Microeng. **15**, 1184 (2005).
[34]K. H. Kang, Langmuir **18**, 10318 (2002).
[35]K. H. Kang, I. S. Kang, and C. M. Lee, Langmuir **19**, 5407 (2003).
[36]J. S. Hong, S. H. Ko, K. H. Kang, and I. S. Kang, Microfluid. Nanofluid. **5**, 263 (2008).
[37]A. Greenbaum, *Iterative Methods for Solving Linear Systems* (Society for Industrial and Applied Mathematics, Philadelphia, PA, 1997).
[38]W. Hackbusch, *Multi-Grid Methods and Applications* (Springer-Verlag, Berlin, NY, 1985).
[39]T. A. Davis, ACM Trans. Math. Softw. **30**, 196 (2004).
[40]T. B. Jones, J. D. Fowler, Y. S. Chang, and C.-J. Kim, Langmuir **19**, 7646 (2003).
[41]R. Baviere, J. Boutet, and Y. Fouillet, Microfluid. Nanofluid. **4**, 287 (2008).
[42]V. Bahadur and S. V. Garimella, J. Micromech. Microeng. **16**, 1494 (2006).
[43]J. Berthier, P. Dubois, P. Clementz, P. Claustre, C. Peponnet, and Y. Fouillet, Sens. Actuators, A **134**, 471 (2007).
[44]F. Brochard, Langmuir **5**, 432 (1989).
[45]R. S. Subramanian, N. Moumen, and J. B. McLaughlin, Langmuir **21**, 11844 (2005).